The effect of slag chemistry on CO_2 binding capacity of C_3S-slag (-gypsum) system

Zhang, Yu; Çopuroğlu, Oğuzhan

DOI
10.1016/j.conbuildmat.2022.129208

Publication date
2022

Document Version
Final published version

Published in
Construction and Building Materials

Construction and Building Materials 354 (2022) 129208

Contents lists available at ScienceDirect

Construction and Building Materials

journal homepage: www.elsevier.com/locate/conbuildmat

The effect of slag chemistry on CO_2 binding capacity of C_3S-slag (-gypsum) system

Yu Zhang *, Oğuzhan Çopuroğlu

Microlab, Section Materials and Environment, Faculty of Civil Engineering and Geosciences, Delft University of Technology, Delft, the Netherlands

ARTICLE INFO

Keywords:
C_3S-slag (-gypsum) system
Slag chemistry
CO_2 binding capacity
TG-DTG-MS

ABSTRACT

In this paper, the authors investigated the correlation between slag chemistry and CO_2 binding capacity of the blended system. To simplify the composition of mixture, model paste containing C_3S, slag covering the common composition range and gypsum was employed.

After accelerated carbonation test, three CO_2-binding phases were identified in the system as: carbonated Ca-Al AFm phases, carbonated hydrotalcite-like phase, and calcium carbonate, irrespective of slag chemistry and the addition of gypsum. On the other hand, carbonated Ca-Al AFm phases played a minor role in absorbing CO_2, sharing less than 5% of CO_2 among all carbonate phases. Hydrotalcite-like phase was able to bind up to ~10% CO_2, depending on the Mg/Al atomic ratio of raw slag. $CaCO_3$, originated from the carbonation of portlandite and C−S−H gel phase, took up more than 85% CO_2 after carbonation. Moreover, the carbonation degree of C−S−H gel phase was found to be negatively related with the Al_2O_3 content and Ca/Si ratio of raw slag.

1. Introduction

Blast furnace slag (slag in short) is a by-product from the production of pig iron. It is formed from the combination of limestone fluxes, coke ashes and residues from iron ore in the furnace and can be simplified as a CaO-SiO_2-Al_2O_3-MgO system. It has been employed as a mature addition in cement industry for several decades, especially in the European and North American countries [1–4].

Cement-based composites blended with slag often exhibits a high resistance to chemical attack, such as alkali silica reaction, sulfate and chloride [5,6]. However, when referring to carbonation resistance, a general decrease is observed compared to pure cement system [7]. It also appears that the reduced carbonation resistance can lead to a serious surface deterioration.

It is well accepted that the carbonation resistance of cementitious materials mainly depends on their pore structure (CO_2 diffusion) and CO_2 binding capacity. The generally higher carbonation rate of slag cement paste is partially due to its lower amount of calcium hydroxide, which is consumed in the pozzolanic reaction with slag [8–12]. Portlandite, as the main CO_2-binding phase, is able to delay the decalcification of another hydration product, C−S−H gel phase [9,13,14]. It is the first hydrate that decomposes to calcium carbonate during carbonation, leading to a moderate volume increase as the molar volume of calcite (36.9 cm^3/mol) is greater than that of portlandite (33.0 cm^3/mol) [15]. This process occurs as a consequence of a dissolution–precipitation reaction and the reaction kinetic is initially more rapid than the carbonation of C−S−H gel phase [16]. Calcium carbonate grows on the surface of portlandite, and the further carbonation is slowed down by the limiting transport of water and CO_2 [17,18]. After all accessible portlandite is consumed, C−S−H gel phase starts to decalcify. A two-step decalcification process of C−S−H gel phase is predicted [19,20]. The first step is a gradual decalcification of the C−S−H gel phase where calcium is removed from the interlayer and defect sites in the silicate chains until Ca/Si = 0.67 is reached, ideally corresponding to infinite silicate chains. In the second step, calcium from the principal layers is consumed, resulting in the final decomposition of the C−S−H gel phase and the formation of an amorphous silica phase. The main carbonation product of C−S−H gel phase is calcium carbonate, which can precipitate in different crystalline polymorphs: calcite, aragonite and vaterite, depending on the internal concrete conditions [21], and the presence of impurities or additives [22,23]. During the hydration process of cement-slag system, C−S−H gel phase with a lower Ca/Si ratio is produced [24–26], which is more easily carbonated, reaching the critical Ca/Si ratio of 0.67 [19,27,28]. Moreover, the comparatively low alkalinity of pore solution in slag cement paste also accelerates carbonation as the rate of carbonation is slower in

* Corresponding author.
E-mail address: Y.Zhang-28@tudelft.nl (Y. Zhang).

https://doi.org/10.1016/j.conbuildmat.2022.129208
Received 12 July 2022; Received in revised form 19 August 2022; Accepted 14 September 2022
Available online 19 September 2022

Table 1
Chemical compositions (wt.%) determined by XRF and physical properties of these eight synthetic slags.

	M0	M8	M16	CS1	CS2	A3	A12	A18
CaO	43.16	37.04	34.09	**32.98**	**28.05**	42.07	37.32	36.87
SiO_2	42.99	37.79	32.99	**38.67**	**42.84**	43.30	39.11	34.43
Al_2O_3	13.30	14.51	15.05	14.51	17.12	**3.69**	**12.32**	**18.19**
MgO	**0.33**	**8.83**	**16.07**	11.22	9.67	10.83	9.43	7.98
FeO/Fe_2O_3	0.07	0.28	0.34	0.36	0.35	0.07	0.30	0.40
TiO_2	–	0.70	0.73	1.02	0.89	–	0.70	0.84
MnO/Mn_2O_3	–	0.17	0.16	0.22	0.19	–	0.15	0.27
Na_2O	–	0.24	0.22	0.36	0.31	–	0.24	0.37
K_2O	–	0.25	0.21	0.36	0.32	–	0.21	0.41
SO_3	0.01	0.01	0.01	0.05	0.08	0.01	0.03	0.03
Residual	0.14	0.18	0.13	0.25	0.08	0.03	0.19	0.21
$(CaO + MgO)/SiO_2$ [a]	1.01	1.21	1.52	1.14	0.88	1.22	1.20	1.30
d_{50} (μm) [b]	24.35	22.73	22.29	20.40	20.11	19.67	20.35	20.85
SSA (m^2/g) [c]	0.77	0.90	0.96	0.93	1.08	1.09	0.92	0.90

a. The European Standard EN 15167–1 recommends that the ratio should be greater than 1.
b. The particle size distribution (PSD) of these slags was measured by EyeTech, Ankersmid.
c. The specific surface area (SSA) of these slags was measured by nitrogen adsorption with the BET method.

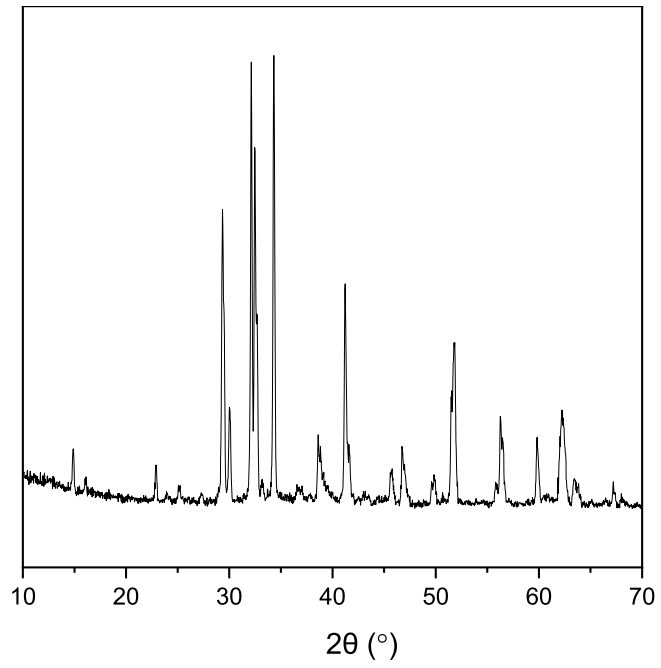

Fig. 1. XRD scan of C_3S used in the present research.

Table 2
Composition (wt.%) of the mixture.

Group	C_3S	Gypsum	Slag	$SO_3/(C_3S +$ gypsum)	Slag/($C_3S +$ gypsum)
I	30	0	70	0	7/3
II	26.775	3.225	70	5 %	7/3

high alkali cement due to the higher CO_2 binding capacity [29]. Although a lower permeability is generally obtained by proper curing in slag cement paste (lower CO_2 diffusion coefficient), the reduction in CO_2 binding capacity because of the decrease of portlandite content and alkalinity of pore solution dominates over the pore refinement [13,30].

As above mentioned, CO_2 binding capacity of slag cement paste is of high importance for predicting its carbonation potential. However, the effect of slag chemistry on CO_2 binding capacity has not been experimentally determined previously, and such information is still scarce both for industry and academia. Therefore, the authors attempted to figure out the correlation between slag chemistry and CO_2 binding capacity of the blended system in this study. To simplify the composition of mixture, model paste containing C_3S ($3CaO•SiO_2$), slag covering the common composition range (synthesized in the laboratory) and gypsum was employed. As the major constituent of cement, C_3S dominates the properties of the hardened paste. Understanding the carbonation behavior of this model paste helps generate a fundamental insight into the carbonation performance of real slag cement. It was found that calcite, aragonite, and vaterite were inhomogeneously formed in the CO_2-contaminated C_3S pastes [31]. C−S−H gel phase of reduced Ca/Si ratio and increased silicate polymerization was also formed during the early stages of carbonation [16]. Additionally, it was concluded that the carbonation rate of C_3S paste was actually controlled by the solution environment [32].

To accelerate the carbonation process, the specimen was ground to powder after 3 months of sealed curing. The carbonation mechanism was investigated through a complementary set of analytical methods, and TG-DTG-MS was employed to quantify the CO_2 binding capacity of each mixture. Meanwhile, the effect of slag composition on absorbing CO_2 was discussed. Collectively, the conclusions obtained in the paper could contribute to designing slag rich concrete structure with improved carbonation resistance (i.e., enhanced CO_2 binding capacity).

2. Material and methodology

2.1. Sample information

Analytically regent C_3S and gypsum were employed in the present paper to produce C_3S-slag (-gypsum) system. Eight synthetic slags (M0, M8, M16, CS1, CS2; A3, A12, A18) covering the common composition range were produced in the laboratory. For detailed production process, please refer to [33].

Chemical composition of slag measured by X-ray fluorescence (XRF) is presented in Table 1. For slag M0, M8, and M16, CaO/SiO_2 ratio was kept at around 1.0 and the amount of Al_2O_3 fluctuated at around 14.0 wt %, while MgO content were determined from 0.33 to 16.07 wt%. Similarly, for slag A3, A12 and A18, CaO/SiO_2 ratio was also maintained at around 1.0 and the amount of MgO was stabilized at about 10.0 wt%, while Al_2O_3 content varied from 3.69 to 18.19 wt%. As for slag CS1 and CS2, the MgO and Al_2O_3 contents levelled-off at approximately 10.0 wt % and 15.0 wt%, respectively, while the CaO/SiO_2 ratio reduced to less than 1.0.

For other properties, e.g., particle size distribution (PSD) and X-ray diffraction result, readers could also refer to [33]. In general, these slags presented a similar properties except for the difference in chemical composition. X-ray diffraction measurement of C_3S is illustrated in

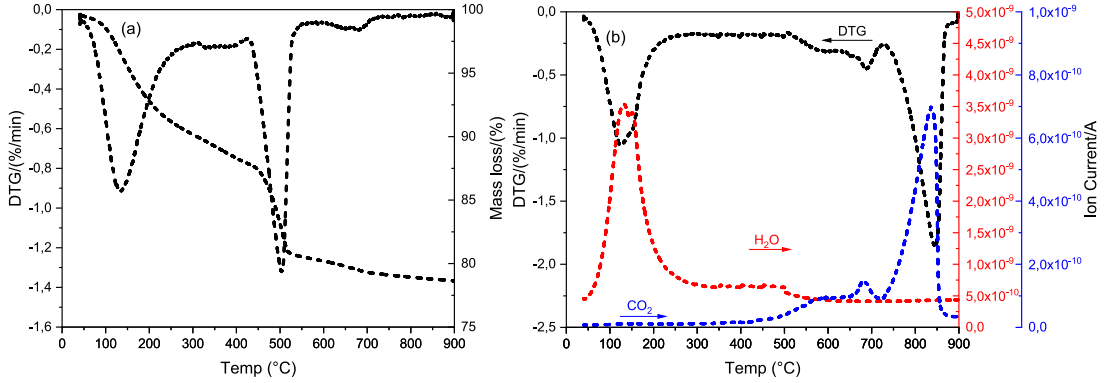

Fig. 2. (a) TG and DTG results of C_3S paste after 3 months of curing; (b) DTG result, H_2O and CO_2 MS curves of hydrated C_3S powder after carbonation.

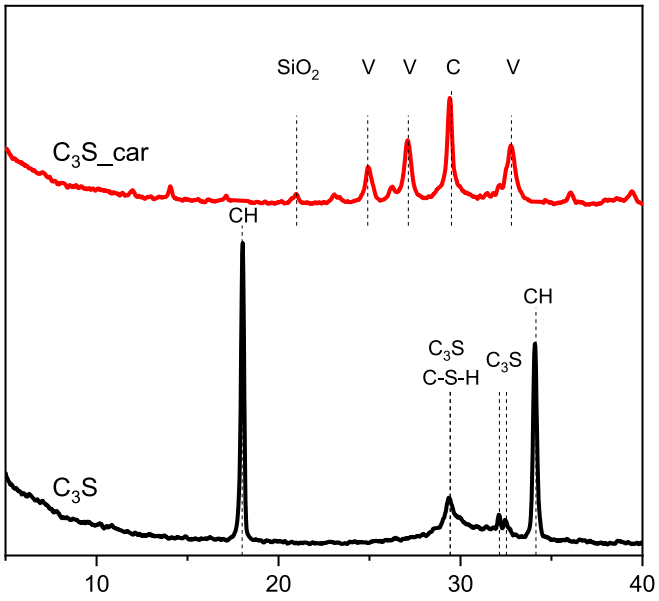

Fig. 3. XRD analysis of C_3S paste after curing of 3 months and hydrated C_3S powder after carbonation. CH: portlandite; C: calcite; V: vaterite.

Fig. 1, and it indicates that C_3S used in this article shows a triclinic polymorph.

2.2. Experimental method

A summary of the specimens prepared for the investigation is listed in Table 2. The substitution level of C_3S was 70 wt% to address the impact of slag, and the water to binder ratio was 0.4. Group I consisted of slag M0, M8, M16, CS1, and CS2 mixtures. The main target of this group was to examine the effect of MgO content and CaO/SiO_2 ratio of slag on CO_2 binding capacity of the blended system. As for Group II, gypsum was incorporated by replacing C_3S, and it was comprised of slag A3, A12, and A18 mixtures. This group was designed to manifest the interaction between alumina of slag and gypsum, and its influence on CO_2 binding capacity. Paste was prepared and cast in the plastic bottle of 20 mL, which was sealed with thin para film on the seal to avoid any ingress of CO_2 and evaporation of vapor, and stored in the laboratory for further study.

After 3 months of curing, specimens were demoulded, and slices cut from the specimens were ground and meshed to powder below 63 μm, allowing full carbonation on a practical time scale [34]. Then, powders of each mixture were evenly distributed over a Petri dish and exposed in the CO_2 chamber directly. Accelerated carbonation test was performed in the carbonation chamber regulated by CO_2 concentration of 3% ± 0.2, at 20 ± 3 °C and 65 ± 5% of relative humidity (RH) (using saturated $NaNO_2$ solution). The carbonation age was up to one month to ensure full carbonation.

After the accelerated carbonation test, powders were immersed in isopropanol solution to exchange water and stored in the vacuum for further tests. To identify phases formed before and after carbonation, X-ray diffraction (XRD) and thermogravimetric analysis (TGA) were performed. XRD data was collected using a Philips PW 1830/40 Powder diffractometer with Cu K-alpha radiation. The machine was operated with an X-ray beam current of 40 mA and an acceleration voltage of 40 kV. Sample powders were scanned from 5 to 60° (2θ) with a step size of 0.03°. TGA was performed on Netzsch STA 449 F3 Jupiter coupled with mass spectrometer (MS) Netzsch QMS 430C under Argon atmosphere. The emission of H_2O and CO_2 from sample after heating was thus identified. About 50 mg sample powder was heated from 40 to 900 °C with a heating rate of 10 °C/min in an Al_2O_3 crucible with an identical and blank one as reference.

Fourier transform infrared spectroscopy (FTIR) was carried out using Spectrum TM 100 Optical ATR-FTIR spectrometer over the wavelength range from 600 to 4000 cm^{-1} to characterize the alteration of molecule structure before and after accelerated carbonation test. A single-beam configuration was used, and each sample was scanned 20 times with a fixed instrument resolution of 4 cm^{-1}.

Polished section was prepared for microanalysis. A FEI QUANTA FEG 650 ESEM equipped with energy dispersive X-ray spectroscopy detector was employed in high vacuum chamber condition to characterize phases in the matrix with internal standard (standardless microanalysis). All microanalysis was carried out at a working distance of 10 mm and an accelerating voltage of 10 kV, respectively.

3. Results

3.1. Carbonation product

3.1.1. Pure C_3S system

It is well recognized that the hydration of C_3S follows the following equation [35,36], and its main precipitations are nanocrystalline/amorphous C−S−H gel phase jointly with the crystallization of portlandite, $Ca(OH)_2$. It is noted that × is the Ca/Si atomic ratio and y is the amount of water bound in C−S−H gel phase.

$$3CaO \bullet SiO_2 + (3 - x + y)H_2O \rightarrow xCaO \bullet SiO_2 \bullet yH_2O + (3 - x)Ca(OH)_2$$

Fig. 2(a) presents the TG and DTG curves of C_3S paste after 3 months of sealed curing. There were two distinct endothermic peaks on the DTG curve, corresponding to the water loss of C−S−H gel phase between 100 and 150 °C and the dehydroxylation of portlandite between 400 and 500 °C.

Fig. 2(b) illustrates the DTG result, H_2O and CO_2 MS curves of

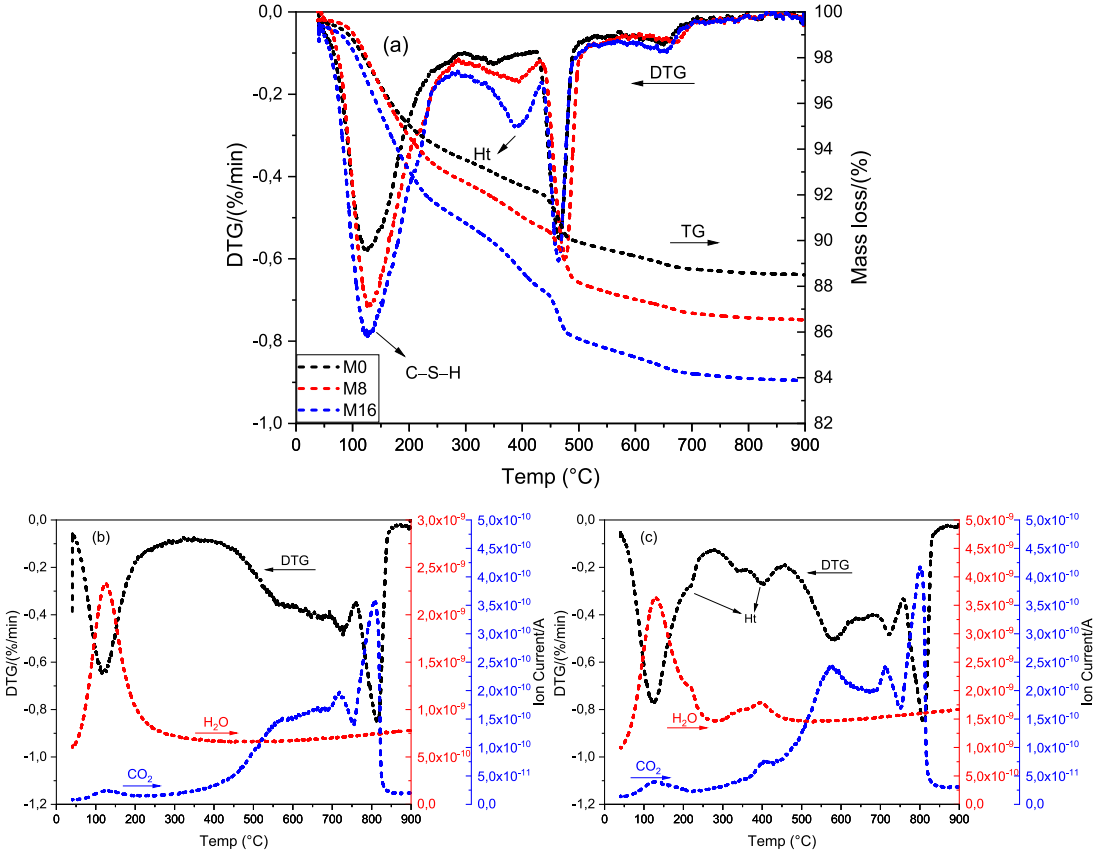

Fig. 4. (a) Representative TG and DTG results of C_3S-slag pastes after 3 months of curing; DTG result, H_2O and CO_2 MS curves of hydrated (b) slag M0 and (c) slag M16 powders after carbonation.

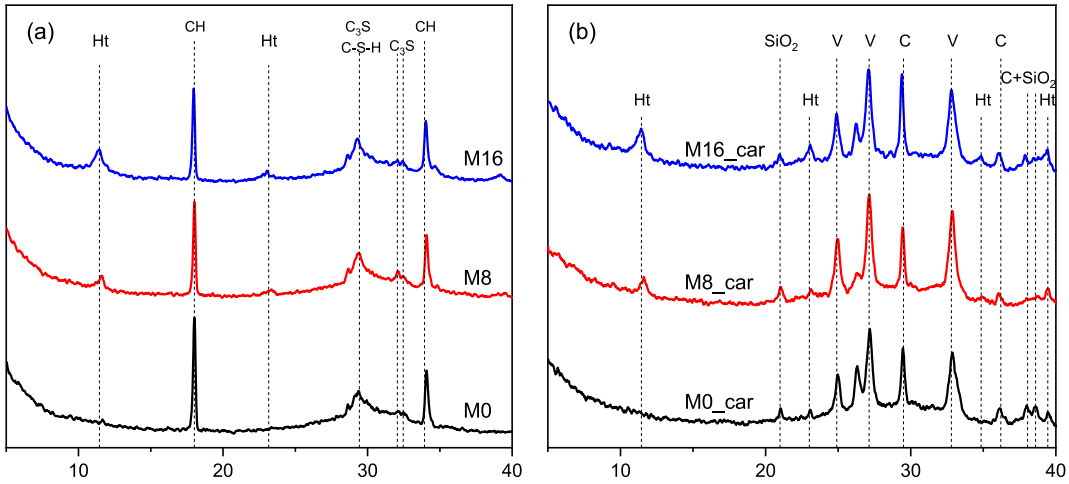

Fig. 5. Representative XRD analysis of (a) C_3S-slag pastes after 3 months of curing and (b) hydrated powders after carbonation. Ht: hydrotalcite-like phase; CH: portlandite; C: calcite; V: vaterite.

hydrated C_3S powder after accelerated carbonation test. The main CO_2-binding phase was calcium carbonate, the decomposition peak of which started from around 500 °C in the DTG graph. These peaks implied the presence of different morphologies of calcium carbonate, including amorphous calcium carbonate, aragonite and/or vaterite, and calcite in particular, which were commonly seen in the accelerated carbonation test of cementitious materials [37–39]. The peak at 100–150 °C suggested the persistence of C−S−H gel phase, although its Ca/Si ratio had decreased remarkably due to the removal of calcium atom from silicate chain [19,20,40].

XRD results (Fig. 3) reveal the presence of portlandite and minor unhydrated C_3S particles in pure C_3S system at 90 days. For C−S−H gel phase, the main peaks were located at around (2θ =) 30° (see PDF 034–0002 and 033–0306), which was very difficult to distinguish from that of C_3S. On the other hand, the peak for portlandite vanished after accelerated carbonation test, meaning that all of it had been carbonated and transformed into calcium carbonate, in agreement with the results determined by TGA (Fig. 2(b)). Additionally, the peak for unhydrated

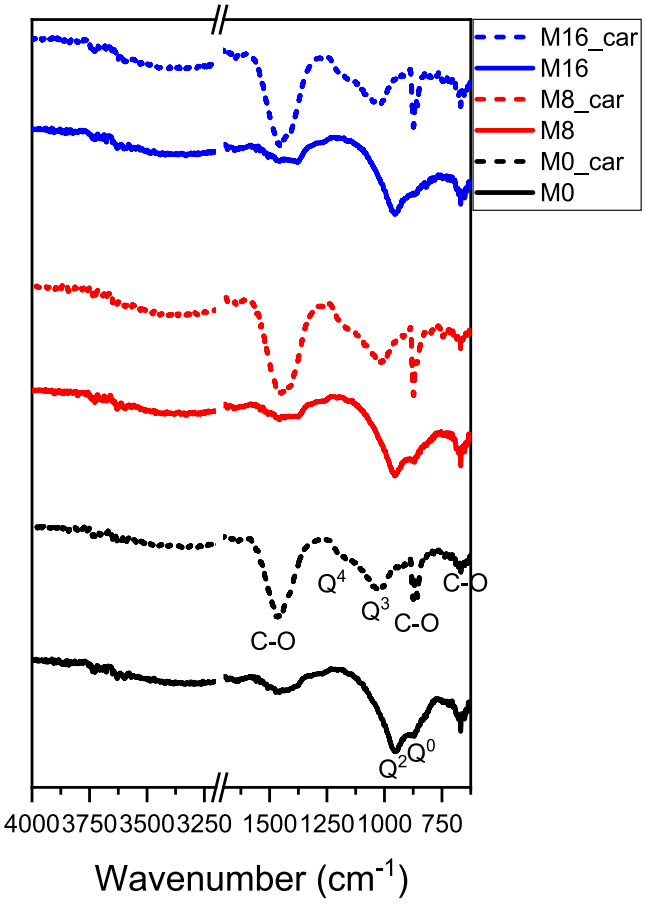

Fig. 6. Representative FTIR spectra of C_3S-slag pastes after 3 months of curing and hydrated powders after carbonation (Normalized, %).

C_3S particle also disappeared, probably associated with its continuous hydration or carbonation.

The small hump centered at around 21° was related to the formation of poorly ordered silica gel due to the carbonation of C−S−H gel phase [9]. Calcite and vaterite were identified as the main polymorphs of $CaCO_3$. No trace of aragonite was found by XRD. The intensified peak at ~800 °C in the DTG curve in Fig. 2(b) also indicated the mass precipitation of calcite. The results in [41] pointed out that compared with aragonite, vaterite was formed preferentially on the surface of portlandite due to their similar symmetries and positive surface charge. Also, the environment in the carbonation chamber (low temperature, i.e., ~20 °C in the present study) favored the coexistence of vaterite and calcite [42].

3.1.2. C_3S-slag system

With the gradual addition of slag, portlandite, the main hydration product of C_3S, reacts with slag and contributes to the formation of C−S(A)−H gel phase and hydrotalcite-like phase, as the following equation demonstrates [43,44]. Five slags with different chemical compositions were employed to produce C_3S-slag system in this study, namely slag M0, M8, M16, CS1, and CS2 mixtures.

$$Slag + Ca(OH)_2 + H_2O \rightarrow C-S(A)-Hgelphase + Hydrotalcite-like\ phase$$

TG-DTG-MS

Compared with the hydration of pure C_3S, two evident differences occurred in the DTG curve of C_3S-slag system (Fig. 4(a)). One was the reduction of portlandite content implied by the intensity of peak between 400 and 500 °C. The other one was the precipitation of hydrotalcite-like phase with a tiny shoulder and a distinct peak located at approximately 250 and 350 °C, respectively. As a Mg-Al Layered Double Hydroxides, its amount was positively related to the MgO content of slag. Thus, the most hydrotalcite-like phase was detected in slag M16 mixture while there was nearly no hydrotalcite-like phase formed in slag M0 mixture.

Representative DTG results, H_2O and CO_2 MS curves of carbonated slag M0 and M16 powders are plotted in Fig. 4(b and c), respectively. Similarly, the main CO_2-binding phase was calcium carbonate, and decomposition peaks after 500 °C in the DTG graph suggested the presence of various morphologies of $CaCO_3$. The peak located at 300–450 °C indicated the persistence of hydrotalcite-like phase after carbonation (Fig. 4(c)). As displayed in the MS curves, both H_2O and CO_2 were liberated from this phase after heating, meaning that both H_2O and CO_2 were absorbed in the interlayer space due to its stacked layer structure [45–47]. Conversely, no hydrotalcite-like phase was formed in slag M0 mixture, thus there was no release of H_2O nor CO_2 at 300–450 °C in this mixture (Fig. 4(b)). As for the small peak at ~150 °C in the MS CO_2 curve, it can be ascribed to the release of CO_2 from carbonated Ca-Al AFm phases (amorphous or nano-crystalline) owing to the carbonation of e.g., AFm-OH phase.

XRD

Representative XRD results (Fig. 5(a)) reveal the presence of hydrotalcite-like phase, portlandite, and unhydrated C_3S clinker in C_3S-slag system after hydration. The intensity of peak indicating portlandite became weaker with the gradual addition of MgO in slag, suggesting a higher reactivity of slag with more MgO incorporation, and thus more portlandite was consumed in the pozzolanic reaction with slag. Also, the peak for hydrotalcite-like phase was much more visible in slag M16 blend, consistent with the results measured by TGA (Fig. 4(a)).

After accelerated carbonation test, the peak for portlandite disappeared in all mixtures. Hydrotalcite-like phase was still observed after such a heavy CO_2 attack (Fig. 5(b)), consistent with the results examined by TGA (Fig. 4(c)). Similar to the carbonation products of pure C_3S system, calcite and vaterite were identified as the main polymorphs of $CaCO_3$ in these pastes.

FTIR

FTIR was also used to check the carbonation products of C_3S-slag system, especially the alteration of C−S−H gel phase at molecular level. Fig. 6 displays the FTIR spectra of representative mixtures before and after carbonation. Commonly, positions of silicate group in FTIR spectra suggest the presence of different molecular structures of C−S−H gel phase. Depending on the connectivity of silicon site in the $[SiO_4]^{4-}$ tetrahedral, silicate tetrahedral can be divided into five characteristic units further with representative IR absorption bands separately, in terms of Q^4 (~1200 cm^{-1}), Q^3 (~1100 cm^{-1}), Q^2 (~950 cm^{-1}), Q^1 (~900 cm^{-1}), and Q^0 (~850 cm^{-1}), respectively [48–51]. Regardless of slag chemistry, Q^2 was the main unit of C−S−H gel phase of all investigated pastes after hydration. After carbonation, the Si-O-T stretching band was characterized by signals appearing at ~1200 and ~1100 cm^{-1}, which was linked with the yield of Q^4 and Q^3 silicate units, respectively. No doubt, this shift was associated with the gradual polymerization of silicate units due to the carbonation-induced decalcification of C−S−H gel phase [52–54].

The carbonation was also confirmed through three types of carbonate bands observed in the FTIR spectra, i.e., strong broad band at 1400–1500 cm^{-1}, representing the asymmetric stretching of carbonate, narrow band at 875–1000 cm^{-1} due to the bending of carbonate, and in-plane bending of carbonate at ~710 cm^{-1} [41].

3.1.3. C_3S-slag-gypsum system

With the addition of gypsum, aluminum dissolved from slag (in the form of AlO_2^-) reacts with SO_4^{2-} ion from gypsum and participates into ettringite as the following equation shows [55,56]. Moreover, ettringite transforms into calcium monosulfoaluminate with the gradual supply of alumina from slag. To investigate their effects on capturing CO_2, three slags with different chemical compositions (different alumina contents)

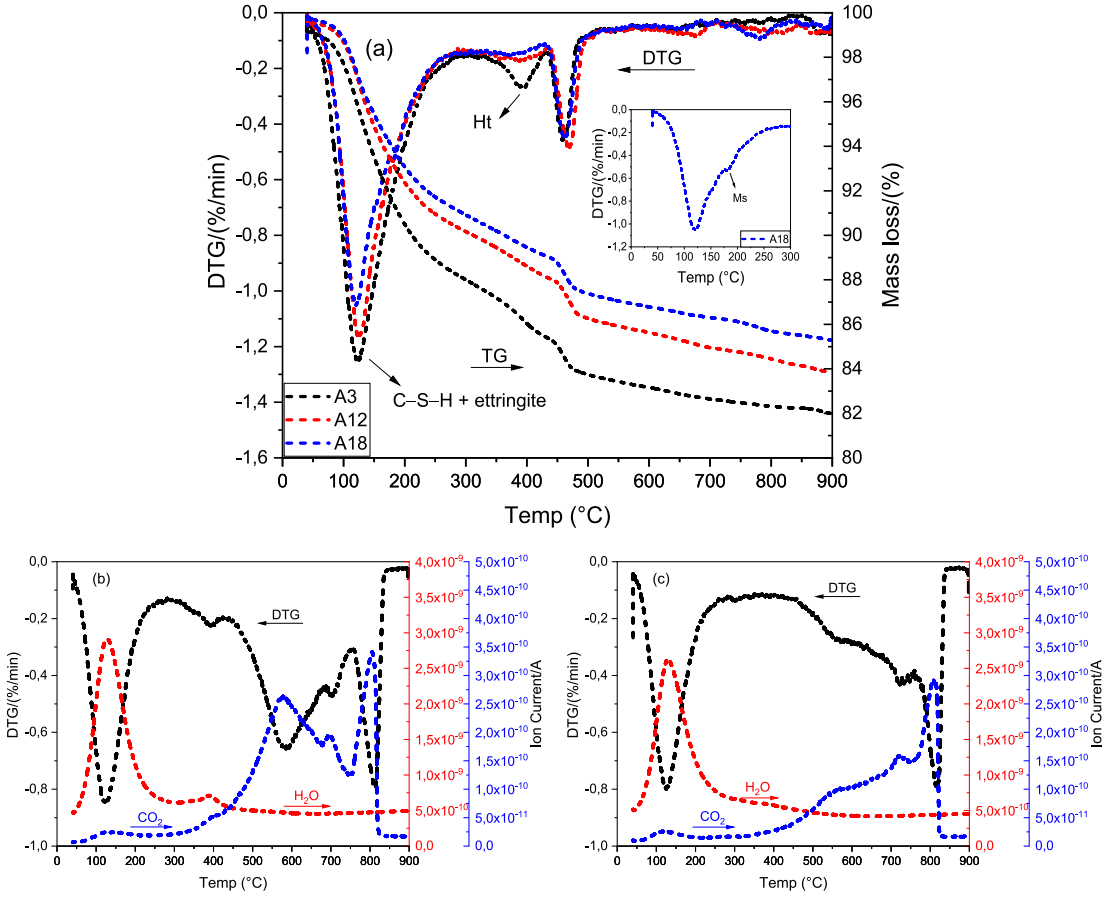

Fig. 7. (a) TG and DTG results of C_3S-slag-gypsum pastes after 3 months of curing; DTG result, H_2O and CO_2 MS curves of hydrated (b) slag A3 and (c) slag A18 powders after carbonation. Ms: calcium monosulfoaluminate; Ht: hydrotalcite-like phase.

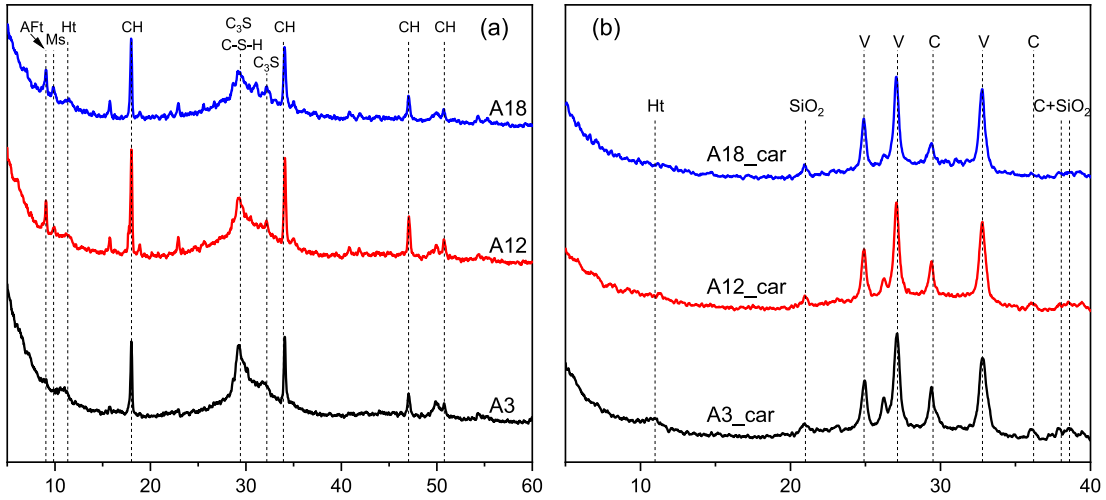

Fig. 8. XRD analysis of (a) C_3S-slag-gypsum pastes after curing of 3 months and (b) hydrated powders after carbonation. AFt: ettringire; Ms: calcium monosulfoalunimate; Ht: hydrotalcite-like phase; CH: portlandite; C: calcite; V: vaterite.

were used to produce C_3S-slag-gypsum system (Group II shown in Table 2), namely slag A3, A12, and A18 mixtures.

$$6Ca^{2+} + 2AlO_2^- + 3SO_4^{2-} + 4OH^- + 30H_2O \rightarrow Ca_6Al_2(SO_4)_3(OH)_{12} \bullet 26H_20$$

$$Ca_6Al_2(SO_4)_3(OH)_{12} \bullet 26H_20 + 6Ca^{2+} + 8OH^- + 4AlO_2{}^- \rightarrow 3Ca_4Al_2(SO_4)(OH)_{12} \bullet 6H_20$$

TG-DTG-MS

Compared with the hydration of C_3S-slag mixture, two evident differences occurred in the DTG curve of C_3S-slag-gypsum system (Fig. 7 (a)). One was presence of ettringite. Although the decomposition peaks for C−S−H gel phase and ettringite overlapped in 100–150 °C, this peak became much sharper and more intensified in gypsum-containing system due to the formation of ettringite. The other one was the

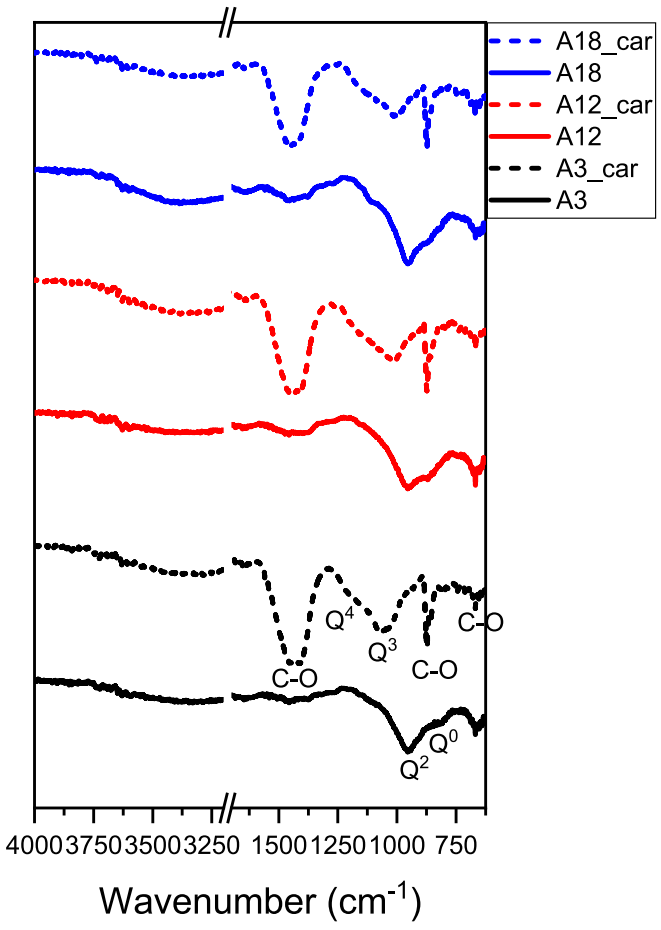

Fig. 9. FTIR spectra of C_3S-slag-gypsum pastes after 3 months of curing and hydrated powders after carbonation (Normalized, %).

precipitation of calcium monosulfoaluminate with a tiny shoulder located at approximately 200 °C, as shown in the insert graph. Its occurrence was associated with the Al_2O_3 content of slag, and together with the results of XRD (Fig. 8(a)), calcium monosulfoaluminate was only detected in slag A12 and A18 mixtures. Besides, note that the peak for hydrotalcite-like phase almost vanished in slag A18 mixture although it contained 7.98 wt% MgO.

On the other hand, the DTG results, H_2O and CO_2 MS curves of carbonated slag A3 and A18 powders are plotted in Fig. 7(b and c), respectively. Still the main CO_2-binding phase was calcium carbonate. The peak located at 300–500 °C indicated the persistence of hydrotalcite-like phase after carbonation in slag A3 blend.

XRD

Besides portlandite and unhydrated C_3S, XRD scans (Fig. 8(a)) reveal the presence of ettringite and calcium monosulfoaluminate in slag A12 and A18 blends due to the addition of gypsum. It also deserved to be mentioned that there was few ettringite and calcium monosulfoaluminate detected by XRD in slag A3 blend because of its low alumina content.

Meanwhile, the addition of gypsum seemed to exert no effect on the mineralogy of carbonation product, which was almost the same to that of C_3S-slag system (Fig. 5(b)). The peak for ettringite and calcium monosulfoaluminate disappeared totally after carbonation, and the possible intermediates, e.g., hemi- and/or mono-carboaluminate as the carbonation products of ettringite and calcium monosulfoaluminate [57], were also not detected in these three mixtures in the present research.

FTIR

As Fig. 9 shows, FTIR spectra of C_3S-slag-gypsum mixture presents a similar characteristic to that of mixtures without gypsum before and after carbonation. Q^2 was the main unit of C–S–H gel phase of blended paste after hydration. After carbonation, the Si-O-T stretching band shifted left to ~1200 and ~1100 cm^{-1}, indicating the formation of Q^4 and Q^3 silicate units, respectively.

3.2. The amount of CO_2 bound in different phases

To calculate the CO_2 concentration of each carbonate phase after accelerated carbonation test, pure agent $CaCO_3$ provided by VWR Chemicals BDH was employed as standard under the same analytical condition. Fig. 10(a) shows the DTG result, CO_2 MS curve of pure $CaCO_3$. The area under the MS CO_2 curve corresponding to 44 wt% CO_2 releasing from $CaCO_3$ was determined using commercial software OriginPro 2019.

As confirmed in Section 3.1, calcium carbonate existed in polymorphs after carbonation. They started to decompose from ~500 °C and the decomposition peaks overlapped with each other noticably [37–39]. However, the exact polymorphs of calcium carbonate were not the concern here, and the simultaneous presence of these polymorphs did not affect the determination of total CO_2 bound in calcium carbonate. As for carbonated hydrotalcite-like phase, it releases CO_2 at 250–450 °C, and an apparent decomposition peak is noted in this temperature range [58,59]. Fortunately, no other phases released CO_2 within this range in the carbonated slag cement sample. Therefore, the CO_2 concentration of each carbonate phase at different depths can thus be estimated from the area under the CO_2 MS curve in the corresponding temperature range, using M16 as an example shown in Fig. 10(b). Portlandite and C–S–H gel phase were the main CO_2 binding phases, and their carbonation product was calcium carbonate of different forms. Hydrotalcite-like and

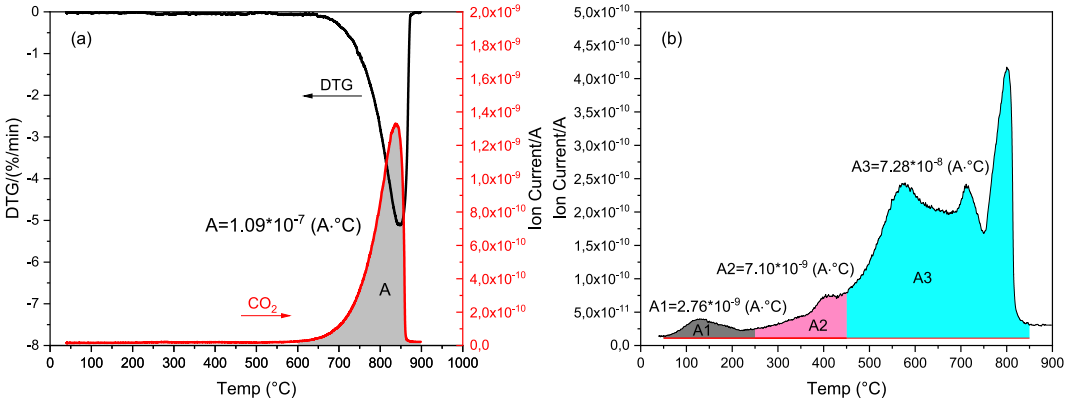

Fig. 10. (a) The DTG result, CO_2 MS curve of pure $CaCO_3$; (b) The CO_2 MS curve of carbonated slag M16 powder.

Table 3
The areas under MS CO_2 curve and the corresponding CO_2 proportions of different carbonate phases.

		Areas under the MS CO_2 curve (A•°C)			Total
		Carbonated Ca-Al AFm phases	Carbonated Hydrotalcite-like phase	Calcium carbonate ($CaCO_3$)	
	Pure $CaCO_3$	–	–	$1.09*10^{-7}$	$1.09*10^{-7}$
	Pure C_3S	–	–	$7.00*10^{-8}$	$7.00*10^{-8}$
Group I	M0	$3.12*10^{-9}$	–	$6.08*10^{-8}$	$6.39*10^{-8}$
	M8	$1.85*10^{-9}$	$4.94*10^{-9}$	$6.04*10^{-8}$	$6.72*10^{-8}$
	M16	$2.76*10^{-9}$	$7.10*10^{-9}$	$7.08*10^{-8}$	$8.06*10^{-8}$
	CS1	$2.13*10^{-9}$	$4.80*10^{-9}$	$6.99*10^{-8}$	$7.69*10^{-8}$
	CS2	$2.07*10^{-9}$	$3.26*10^{-9}$	$6.48*10^{-8}$	$7.02*10^{-8}$
Group II	A3	$2.31*10^{-9}$	$5.54*10^{-9}$	$6.50*10^{-8}$	$7.28/(8.15^{a})*10^{-8}$
	A12	$1.85*10^{-9}$	$3.56*10^{-9}$	$5.29*10^{-8}$	$5.83/(6.53^{a})*10^{-8}$
	A18	$2.63*10^{-9}$	$1.38*10^{-9}$	$4.36*10^{-8}$	$4.76/(5.33^{a})*10^{-8}$
		CO_2 proportion shared by each carbonate phase (%)			CO_2 in the carbonated powder (wt %)
		Carbonated Ca-Al AFm phases	Carbonated Hydrotalcite-like phase	Calcium carbonate ($CaCO_3$)	
	Pure $CaCO_3$	–	–	100	44.00
	Pure C_3S	–	–	100	28.26
Group I	M0	4.88	–	95.12	25.79
	M8	2.75	7.37	89.88	27.12
	M16	3.42	8.85	87.73	32.54
	CS1	2.77	6.25	90.98	31.04
	CS2	2.95	4.64	92.41	28.34
Group II	A3	3.17	7.61	89.22	$29.38/32.91^{a}$
	A12	3.17	6.11	90.72	$23.53/26.36^{a}$
	A18	5.53	2.90	91.57	$19.21/21.52^{a}$

a. Normalized to 30 g C_3S.

Ca-Al AFm phases (including ettringite, AFm-OH, and AFm-SO_4 in this article), due to their stacked layer structures, also absorbed a certain amount of CO_2, forming carbonated hydrotalcite-like phase and carbonated Ca-Al AFm phases, respectively. The area A1, A2, and A3 depicted in Fig. 10(b) corresponded to certain amounts of CO_2 releasing from carbonated Ca-Al AFm phases, carbonated hydrotalcite-like phase, and calcium carbonate, respectively.

As found in Section 3.1, there was no fundamental change of the CO_2-binding phases in C_3S-slag (-gypsum) system after carbonation. The areas under MS CO_2 curve and the corresponding CO_2 proportions shared by different carbonate phases in all investigated samples are summarized and given in Table 3.

As shown in Table 3, the CO_2 bound in C_3S-slag (-gypsum) system was mainly present in calcium carbonate, originated from the carbonation of portlandite and C−S−H gel phase (from the hydration of C_3S and slag both). It was noted that Ca-Al AFm phases played a minor role in absorbing CO_2, sharing less than 5 % of CO_2 among all carbonate phases. With sufficient Al_2O_3, they absorbed a little more than 5 % of CO_2 in slag A18 mixture although the absolute amount (area) levelled off roughly. The role of hydrotalcite-like phase in binding CO_2 started to emerge with the gradual addition of MgO in slag, and the binding ability was positively related to its content after hydration. The most hydrotalcite-like phase was detected in slag M16 paste, and it was able to absorb up to ~9 % CO_2 after full hydration.

4. Discussion

Commonly, it is recognized that CO_2 binding capacity of C_3S-slag (-gypsum) system should be positively related to the reactivity of slag. Although portlandite, one of the main CO_2 absorbing phase, would be consumed in the pozzolanic reaction with slag, secondary precipitations, e.g., Ca-Al AFm phases, hydrotalcite-like phase, and C−S(A)−H gel phase, would also act as CO_2-binding phases. In the previous work [33], we discussed the correlation between slag chemistry and its reactivity. It was found that slag reactivity was favorably affected by increasing Al_2O_3 and MgO contents. In other words, slag M0 and A3 presented low reactivity, while slag M16 and A18 showed high reactivity. However, based on the results present in this study, the correlation between slag chemistry and CO_2 binding capacity of C_3S-slag (-gypsum) system differs.

It is generally accepted that Al_2O_3-rich slag shows high reactivity, as the increased Al_2O_3 content of slag is reported to enhance the reaction involving the formation of ettringite [60–62]. Also, the formation of calcium monosulfoaluminate became increasingly prominent with the gradual incorporation of Al_2O_3 in slag as shown in Fig. 7(a). After carbonation, hemi- and mono-carboaluminate were predicted as the intermediates of its carbonation [57]. However, as confirmed by XRD results (Fig. 8(b)), ettringite and monosulfate disappeared completely after carbonation, and no trace of hemi- or mono-carboaluminate was identified. A possible explanation here was that due to the full carbonation of sample powder, intermediates, including hemi- and mono-carboaluminate, had carbonated further and led to the formation of calcium carbonate and gypsum [14]. On the other hand, gypsum was also not detected by XRD in the study. As for the small peak at ~150 °C in the MS CO_2 curve in all investigated samples, irrespective of the gypsum addition or not, it should be ascribed to the formation of carbonated Ca-Al AFm phases, i.e., from the carbonation of ettringite, AFm-OH and AFm-SO_4 (monosulfate) phases, partially replacing SO_4^{2-} and/or OH^- ions by CO_3^{2-} ion as they also presented a stacked layer structure [63]. Similarly, these carbonate phases cannot be identified by XRD, probably they are amorphous or nano-crystalline. Meanwhile, they only played a minor role in absorbing CO_2, sharing less than 5 % of CO_2 among all carbonate phases as Table 3 and Fig. 11 illustrates.

Additionally, it was noticed that the total CO_2 binding capacity decreased significantly with the increasing Al_2O_3 content from slag A3 to A18 blend (Fig. 11), in contrast to the reactivity of slag as mentioned above. This decline trend was exhibited in three aspects: (1) The CO_2 amount bound in carbonated Ca-Al AFm phases was stable, i.e., the enhanced ettringite and monosulfate formations with increasing alumina content in slag did not exert positive effect on CO_2 binding capacity. (2) The CO_2 content absorbed by hydrotalcite-like phase decreased. In fact, the high Al_2O_3 content of slag suppressed the formation of hydrotalcite-like phase as confirmed in Fig. 7(a), in agreement of results reported in [64,65]. (3) The remarkable decrease of CO_2 amount bound in calcium carbonate. Considering the similar and low amount of portlandite remained at 90 days in these mixtures (Fig. 7(a)), the decrease was more likely to be caused by the reduced carbonation of C−S(A)−H gel phase.

Fig. 12(a and b) show representative BSE images of slag M16 and A18 mixtures at 90 days, respectively. Partially hydrated C_3S grains as well as inner products surrounding the unreacted cores (circled in Fig. 12(a)), and so-called Hadley grains, which hydrated completely to leave hollow hydration shell (circled in Fig. 12(b)) were distributed everywhere, embedded into the matrix together with unhydrated slag particle. Slag particle hydrated slowly, and precipitates as the rims of unhydrated slag particles after 3 months were formed as a whole with

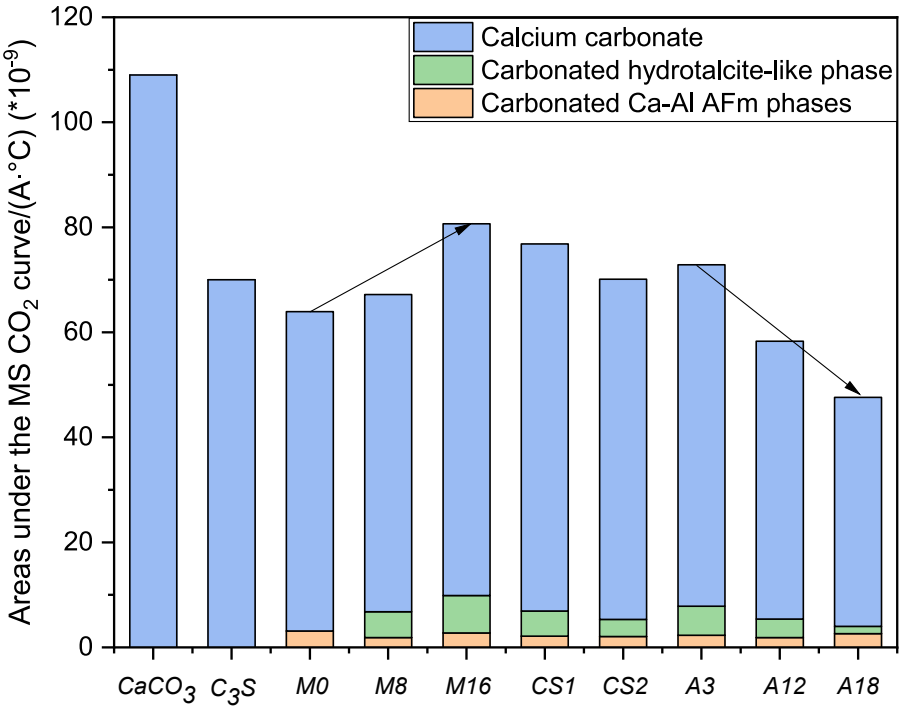

Fig. 11. The areas under MS CO_2 curve corresponding to different carbonate phases.

the surrounding matrix.

Fig. 12(c) illustrates the representative atomic ratio of Al/Ca against Si/Ca of slag M16 and A18 mixtures at 90 days. In fact, The Ca/Si atomic ratio measured in all these samples fluctuated at 1.0–1.1 (except slag CS1 and CS2 mixtures due to their low CaO/SiO_2 ratios of raw slags). However, the values of Al/Si atomic ratio varied considerably among these mixtures. The highest Al/Si ratio was determined in slag A18 mixture, close to 0.20, double of that in slag M16 mixture. It explained the reduced carbonation degree of C−S(A)−H gel phase in slag A18 mixture. For one thing, aluminum uptake in C−S−H gel phase increased the content of bridging silicate tetrahedron [66], and a more polymerized unit commonly exhibited better carbonation resistance [67,68]. For another, coupling a high aluminum content, aluminate of pentahedral and octahedral coordination were produced [19,69]. The pentahedral product was located in the C−S(A)−H interlayers and the octahedral product on its surfaces. The presence of those species correlated with a lower kinetic degradation for C−S(A)−H gel phase by the limited CO_2 access [69].

Based on the *R*3 test results in [33], higher reactivity was observed with the increasing amount of MgO in slag. TGA (Fig. 4) and XRD (Fig. 5) results in this article also suggested that the increasing MgO content in slag effectively favored the formation of hydrotalcite-like phase, consistent with the results in [70–72]. During CO_2 attack, due to its stacked layer morphology, the space between layers presented a large specific surface area comparable to that of C−S−H gel phase [73], and was the natural site to fix CO_2 molecules [74,75]. In all investigated samples, hydrotalcite-like phase was able to absorb up to ~10 % CO_2 at most, and this value was positively associated with the Mg/Al atomic ratio of raw slag as Fig. 13 displays. It thus explained the increasing CO_2 binding capacity with the rising of MgO content in slag. On the other hand, although containing 7.98 wt% MgO, the high Al_2O_3 content in slag A18 suppressed the formation of hydrotalcite-like phase, and thus a low amount of CO_2 was bound in it.

In general, portlandite and C−S−H gel phase (in particular) were the main CO_2-binding phases in cementitious materials, and their carbonation products were calcium carbonate of different forms. In the present research, calcium carbonate took up more than 85 % CO_2 after carbonation. An interesting phenomenon occurred here that the amount of $CaCO_3$ formed in slag CS1 and CS2 mixtures was unexpectedly high, compared to their low CaO contents (Table 1) and relatively low reactivity [33].

Fig. 14 illustrates the representative atomic ratio of Al/Ca against Si/Ca of slag M16 and CS1 mixtures at 90 days. A significant reduction of Ca/Si atomic ratio was measured in slag CS1 mixture, to approximately 0.85 (to around 0.79 in slag CS2 mixture). As confirmed in [19,20], C−S−H gel phase with a lower Ca/Si ratio was decomposed faster than that with a higher Ca/Si ratio. Additionally, it was much easier for C−S−H gel phase with a lower Ca/Si ratio to get full carbonation, i.e., reaching Ca/Si ratio of 0.67 [76]. Due to the low CaO/SiO_2 ratio of raw slag CS1 and CS2, C−S−H gel phase with a much lower Ca/Si atomic ratio was formed in these two mixtures. It explained the high $CaCO_3$ content obtained in slag CS1 and CS2 mixtures after carbonation.

5. Conclusions

Based on C_3S-slag (-gypsum) system, the paper investigated the effect of slag chemistry on CO_2 binding capacity of the blended system. Overall, the mineralogy of carbonation products did not change fundamentally with various slag compositions. The main conclusions drawn were as follows:

- C−S−H gel phase, portlandite, and hydrotalcite-like phase were identified as the main hydrates of C_3S-slag system. With gypsum, ettringite occurred in the system, and calcium monosulfoaluminate was also formed with the continuous supply of alumina from slag.
- After accelerated carbonation test, three CO_2-bearing phases were formed: carbonated Ca-Al AFm phases (amorphous or nanocrystalline), carbonated hydrotalcite-like phase, and calcium carbonate (vaterite and calcite), irrespective of slag chemistry and the addition of gypsum.
- Carbonated Ca-Al AFm phases played a minor role in absorbing CO_2, sharing less than 5% of CO_2 among all carbonate phases. Hydrotalcite-like phase was able to absorb up to ~10% CO_2, and this value was positively associated with the Mg/Al atomic ratio of raw

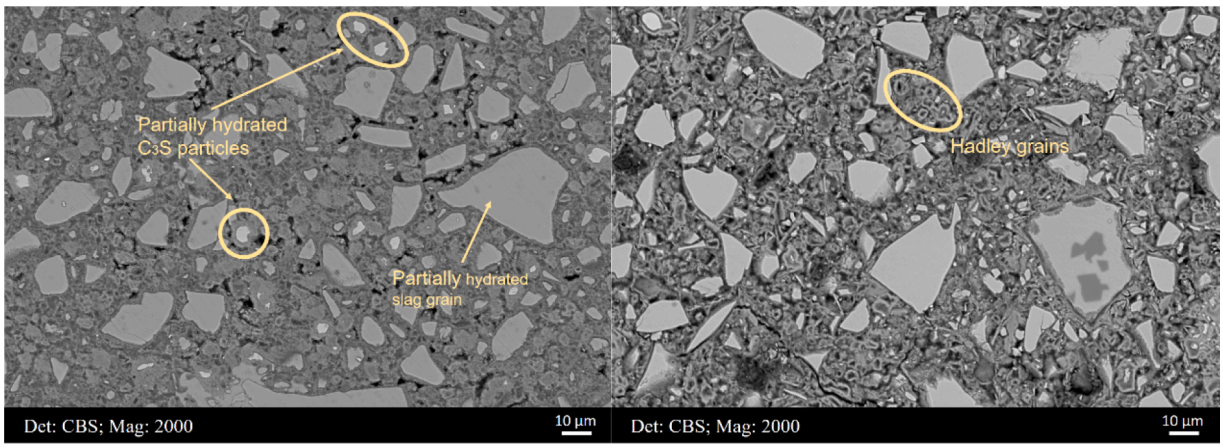

(a) (b)

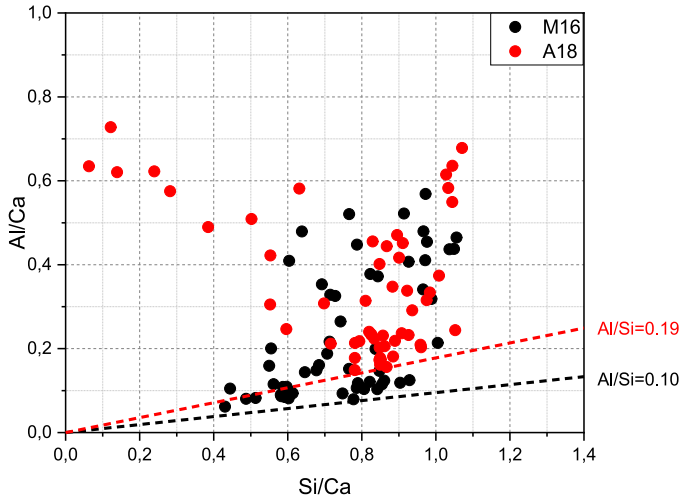

(c)

Fig. 12. (a) and (b) Representative BSE images of slag M16 and A18 mixtures at 90 days, respectively; (c) Atomic ratio of Al/Ca against Si/Ca of slag M16 and A18 mixtures after 3 months of curing.

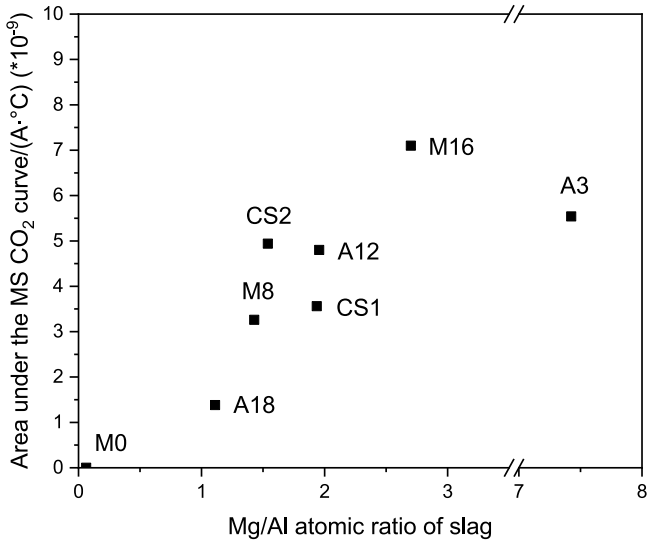

Fig. 13. The area under MS CO_2 curve corresponding to hydrotalcite-like phase vs Mg/Al atomic ratio of raw slag.

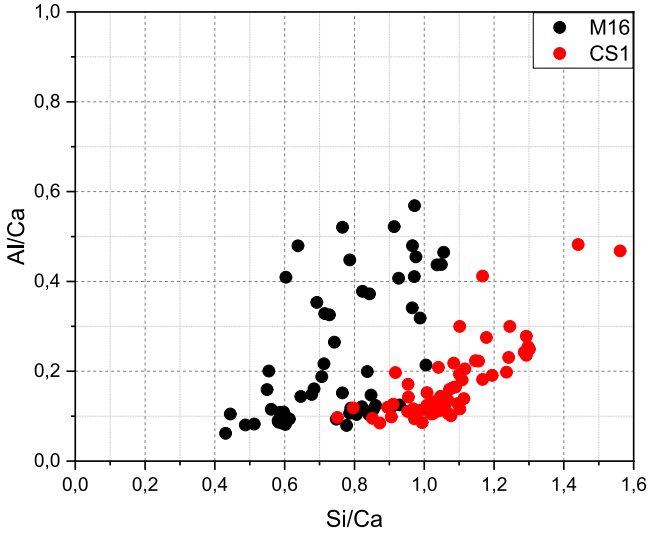

Fig. 14. Atomic ratio of Al/Ca against Si/Ca of slag M16 and CS1 mixtures after 3 months of curing.

slag. $CaCO_3$, originated from the carbonation of portlandite and C−S−H gel phase (in particular), took up more than 85% CO_2 after carbonation.

- Generally, CO_2 binding capacity of C_3S-slag (-gypsum) system was not directly related to the reactivity of slag. System with a Al_2O_3-rich slag presented a low CO_2 binding capacity, while a low CaO/SiO_2 ratio slag contributed to a high CO_2 amount captured in the system.
- Considering the effect of slag chemistry on slag reactivity and CO_2 binding capacity together, high MgO content slag was recommended to design slag rich concrete structure with improved hydration and carbonation resistance performance.

Declaration of Competing Interest

The authors declare that they have no known competing financial interests or personal relationships that could have appeared to influence the work reported in this paper.

Data availability

Data will be made available on request.

Acknowledgements

China Scholarship Council (the Grant Number 201808320456) and BAM Infraconsult B.V. are gratefully acknowledged for their financial support. Authors thank Arjan Thijssen (Microlab, TU Delft) and John van den Berg (Microlab, TU Delft) for their technical support.

References

[1] M. Juenger, et al., Advances in alternative cementitious binders, Cement and Concrete Research 41 (12) (2011) 1232–1243.
[2] E. Crossin, The greenhouse gas implications of using ground granulated blast furnace slag as a cement substitute, Journal of Cleaner Production 95 (2015) 101–108.
[3] Y. Li, et al., Environmental impact analysis of blast furnace slag applied to ordinary Portland cement production, Journal of Cleaner Production 120 (2016) 221–230.
[4] J. Bijen, Benefits of slag and fly ash, Construction and Building Materials 10 (5) (1996) 309–314.
[5] R.B. Polder, T. Nijland, M. de Rooij, Blast furnace slag cement concrete with high slag content (CEM III/B)–Experiences with the durability in The Netherlands since the 1920's, NPRA report SVV 270 (2014) 72.
[6] E. Özbay, M. Erdemir, H.İ. Durmuş, Utilization and efficiency of ground granulated blast furnace slag on concrete properties–A review, Construction and Building Materials 105 (2016) 423–434.
[7] V.G. Papadakis, Effect of supplementary cementing materials on concrete resistance against carbonation and chloride ingress, Cement and Concrete Research 30 (2) (2000) 291–299.
[8] P. Sulapha, et al., Carbonation of concrete containing mineral admixtures, Journal of materials in civil engineering 15 (2) (2003) 134–143.
[9] P.H. Borges, et al., Carbonation of CH and C-S–H in composite cement pastes containing high amounts of BFS, Cement and Concrete Research 40 (2) (2010) 284–292.
[10] Y. Gao, et al., Effects of different mineral admixtures on carbonation resistance of lightweight aggregate concrete, Construction and Building Materials 43 (2013) 506–510.
[11] R. Bucher, et al., Service life of metakaolin-based concrete exposed to carbonation: Comparison with blended cement containing fly ash, blast furnace slag and limestone filler, Cement and Concrete Research 99 (2017) 18–29.
[12] V. Shah, S. Bishnoi, Carbonation resistance of cements containing supplementary cementitious materials and its relation to various parameters of concrete, Construction and Building Materials 178 (2018) 219–232.
[13] B. Wu, G. Ye, Development of porosity of cement paste blended with supplementary cementitious materials after carbonation, Construction and Building Materials 145 (2017) 52–61.
[14] S. von Greve-Dierfeld, et al., Understanding the carbonation of concrete with supplementary cementitious materials: a critical review by RILEM TC 281-CCC, Materials and Structures 53 (6) (2020) 1–34.
[15] Lagerblad, B., *Carbon dioxide uptake during concrete life cycle: State of the art*. 2005: Swedish Cement and Concrete Research Institute Stockholm.
[16] G.W. Groves, et al., Progressive changes in the structure of hardened C3S cement pastes due to carbonation, Journal of the American Ceramic Society 74 (11) (1991) 2891–2896.
[17] I. Galan, et al., Assessment of the protective effect of carbonation on portlandite crystals, Cement and Concrete Research 74 (2015) 68–77.
[18] Ö. Cizer, et al., Real-time investigation of reaction rate and mineral phase modifications of lime carbonation, Construction and Building Materials 35 (2012) 741–751.
[19] T.F. Sevelsted, J. Skibsted, Carbonation of C-S–H and C–A–S–H samples studied by 13C, 27Al and 29Si MAS NMR spectroscopy, Cement and Concrete Research 71 (2015) 56–65.
[20] B. Wu, G. Ye, Study of carbonation rate of synthetic CSH by XRD, *NMR and FTIR*. Heron 64 (1–2) (2019) 21–38.
[21] E. Dubina, et al., Influence of water vapour and carbon dioxide on free lime during storage at 80 C, studied by Raman spectroscopy, Spectrochimica Acta Part A: Molecular and Biomolecular Spectroscopy 111 (2013) 299–303.
[22] C.Y. Tai, F.B. Chen, Polymorphism of CaCO3, precipitated in a constant-composition environment, AIChE Journal 44 (8) (1998) 1790–1798.
[23] L. Fernández-Díaz, Á. Fernández-González, M. Prieto, The role of sulfate groups in controlling CaCO3 polymorphism, Geochimica et Cosmochimica Acta 74 (21) (2010) 6064–6076.
[24] R. Taylor, I. Richardson, R. Brydson, Composition and microstructure of 20-year-old ordinary Portland cement–ground granulated blast-furnace slag blends containing 0 to 100% slag, Cement and Concrete Research 40 (7) (2010) 971–983.
[25] B. Kolani, et al., Hydration of slag-blended cements, Cement and Concrete Composites 34 (9) (2012) 1009–1018.
[26] W. Chen, H. Brouwers, The hydration of slag, part 2: reaction models for blended cement, Journal of Materials Science 42 (2) (2007) 444–464.
[27] X. Liu, et al., Carbonation behaviors of calcium silicate hydrate (CSH): Effects of aluminum, Construction and Building Materials 325 (2022), 126825.
[28] Wu, B. and G. Ye. *Carbonation mechanism of different kind of CSH: rate and products*. in *Int. RILEM Conference on Materials, Systems and Structures in Civil Engineering 2016-Segment on Concrete with Supplementary Cementitious Materials*. 2016. RILEM.
[29] L. Urbonas, V. Leno, D. Heinz, Effect of carbonation in supercritical CO2 on the properties of hardened cement paste of different alkalinity, Construction and Building Materials 123 (2016) 704–711.
[30] H. Justnes, et al., Microstructural changes of hydrated cement blended with fly ash upon carbonation, Cement and Concrete Research 137 (2020), 106192.
[31] J. Ibáñez, et al., Hydration and carbonation of monoclinic C2S and C3S studied by Raman spectroscopy, Journal of Raman Spectroscopy 38 (1) (2007) 61–67.
[32] D. Wang, et al., Growth of calcium carbonate induced by accelerated carbonation of tricalcium silicate, ACS Sustainable Chemistry Engineering 8 (39) (2020) 14718–14731.
[33] Y. Zhang, et al., The effect of slag chemistry on the reactivity of synthetic and commercial slags, Construction and Building Materials 335 (2022), 127493.
[34] S.A. Bernal, et al., Effect of silicate modulus and metakaolin incorporation on the carbonation of alkali silicate-activated slags, Cement and Concrete Research 40 (6) (2010) 898–907.
[35] F. Begarin, et al., Hydration of alite containing aluminium, Advances in Applied Ceramics 110 (3) (2011) 127–130.
[36] B. Mota, T. Matschei, K. Scrivener, The influence of sodium salts and gypsum on alite hydration, Cement and Concrete Research 75 (2015) 53–65.
[37] M. Thiery, et al., Investigation of the carbonation front shape on cementitious materials: Effects of the chemical kinetics, Cement and Concrete Research 37 (7) (2007) 1047–1058.
[38] G. Villain, M. Thiery, G. Platret, Measurement methods of carbonation profiles in concrete: Thermogravimetry, chemical analysis and gammadensimetry, Cement and Concrete Research 37 (8) (2007) 1182–1192.
[39] A. Morandeau, M. Thiery, P. Dangla, Investigation of the carbonation mechanism of CH and CSH in terms of kinetics, microstructure changes and moisture properties, Cement and Concrete Research 56 (2014) 153–170.
[40] R. Hay, J. Li, K. Celik, Phase evolution, micromechanical properties, and morphology of calcium (alumino) silicate hydrates C-(A-) SH under carbonation, Cement and Concrete Research 152 (2022), 106683.
[41] L. Black, et al., Structural features of C-S–H (I) and its carbonation in air—a Raman spectroscopic study. Part II: carbonated phases, Journal of the American Ceramic Society 90 (3) (2007) 908–917.
[42] E.T. Stepkowska, et al., Calcite, vaterite and aragonite forming on cement hydration from liquid and gaseous phase, Journal of thermal analysis calorimetry 73 (1) (2003) 247–269.
[43] W. Chen, H.J.H. Brouwers, The hydration of slag, part 2: reaction models for blended cement, Journal of Materials Science 42 (2) (2006) 444–464.
[44] De Belie, N.e.a., *Properties of fresh and hardened concrete containing supplementary cementitious materials*. Vol. 25. 2018: Springer.
[45] S. Miyata, Physico-chemical properties of synthetic hydrotalcites in relation to composition, Clays and Clay minerals 28 (1) (1980) 50–56.
[46] S. Miyata, Anion-exchange properties of hydrotalcite-like compounds, Clays and Clay minerals 31 (4) (1983) 305–311.
[47] W.T. Reichle, Synthesis of anionic clay minerals (mixed metal hydroxides, hydrotalcite), Solid State Ionics 22 (1) (1986) 135–141.
[48] B.O. Mysen, et al., The influence of TiO2 on the structure and derivative properties of silicate melts, American Mineralogist 65 (11–12) (1980) 1150–1165.
[49] Y. Sun, et al., FTIR, Raman and NMR investigation of CaO–SiO2–P2O5 and CaO–SiO2–TiO2–P2O5 glasses, Journal of Non-Crystalline Solids 420 (2015) 26–33.
[50] G.-H. Kim, I. Sohn, Effect of Al2O3 on the viscosity and structure of calcium silicate-based melts containing Na2O and CaF2, Journal of Non-Crystalline Solids 358 (12–13) (2012) 1530–1537.
[51] S.-M. Han, et al., Surface kinetics of nitrogen dissolution and its correlation to the slag structure in the CaO-SiO2, CaO-Al2O3, and CaO-SiO2-Al2O3 slag system, Journal of Non-Crystalline Solids 357 (15) (2011) 2868–2875.

[52] Y. Okada, et al., Relationship between NMR 29 Si chemical shifts and FT-IR wave numbers in calcium silicates, in: Nuclear Magnetic Resonance Spectroscopy of Cement-based Materials, Springer, 1998, pp. 69–78.
[53] W. Ashraf, J. Olek, Carbonation behavior of hydraulic and non-hydraulic calcium silicates: potential of utilizing low-lime calcium silicates in cement-based materials, Journal of materials science 51 (13) (2016) 6173–6191.
[54] M. Zajac, et al., Kinetics of enforced carbonation of cement paste, Cement and Concrete Research 131 (2020), 106013.
[55] T. Matschei, et al., Thermodynamic properties of Portland cement hydrates in the system CaO–Al2O3–SiO2–CaSO4–CaCO3–H2O, Cement and Concrete Research 37 (10) (2007) 1379–1410.
[56] B. Lothenbach, Thermodynamic equilibrium calculations in cementitious systems, Materials and Structures 43 (10) (2010) 1413–1433.
[57] C.W. Hargis, et al., Carbonation of calcium sulfoaluminate mortars, Cement and Concrete Composites 80 (2017) 123–134.
[58] J.C. Roelofs, et al., *The thermal decomposition of Mg–Al hydrotalcites: effects of interlayer anions and characteristics of the final structure.* Chemistry–A, European Journal 8 (24) (2002) 5571–5579.
[59] J.T. Kloprogge a, J. Kristófb, R.L. Frosta, Thermogravimetric analysis-mass spectrometry (TGA-MS) of hydrotalcites containing CO3 2−, NO3−, Cl−, SO4 2− or ClO4−, Clay Odyssey 1 (2001) 451.
[60] S. Kucharczyk, et al., Structure and reactivity of synthetic CaO-Al2O3-SiO2 glasses, Cement and Concrete Research 120 (2019) 77–91.
[61] S. Kucharczyk, et al., The Influence of Limestone and Al2O3 Content in the Slag on the Performance of the Composite Cements, Procedia Engineering 108 (2015) 402–409.
[62] S. Blotevogel, et al., Ability of the R3 test to evaluate differences in early age reactivity of 16 industrial ground granulated blast furnace slags (GGBS), Cement and Concrete Research 130 (2020), 105998.
[63] Taylor, H.F., *Cement chemistry*. Vol. 2. 1997: Thomas Telford London.
[64] M.B. Haha, et al., Influence of slag chemistry on the hydration of alkali-activated blast-furnace slag — Part II: Effect of Al2O3, Cement and Concrete Research 42 (1) (2012) 74–83.
[65] M. Whittaker, et al., The role of the alumina content of slag, plus the presence of additional sulfate on the hydration and microstructure of Portland cement-slag blends, Cement and Concrete Research 66 (2014) 91–101.
[66] I. Richardson, Tobermorite/jennite-and tobermorite/calcium hydroxide-based models for the structure of CSH: applicability to hardened pastes of tricalcium silicate, β-dicalcium silicate, Portland cement, and blends of Portland cement with blast-furnace slag, metakaolin, or silica fume, Cement and Concrete Research 34 (9) (2004) 1733–1777.
[67] J. Li, et al., Effects of Ca/Si ratio, aluminum and magnesium on the carbonation behavior of calcium silicate hydrate, Materials 12 (8) (2019) 1268.
[68] L. Irbe, et al., The role of aluminium in CASH during chemical attack on concrete. In *Second International Conference on the Chemistry of Construction Materials-ICCCM*, 2016. 2016..
[69] E. Kangni-Foli, et al., Calcium alumino-silicates hydrates (CASH) carbonation kinetics. in *ICCC 2019–15th International Congress on the Chemistry of Cement*, 2019.
[70] M.B. Haha, et al., Influence of slag chemistry on the hydration of alkali-activated blast-furnace slag—Part I: Effect of MgO, Cement and Concrete Research 41 (9) (2011) 955–963.
[71] S.A. Bernal, et al., MgO content of slag controls phase evolution and structural changes induced by accelerated carbonation in alkali-activated binders, Cement and Concrete Research 57 (2014) 33–43.
[72] B. Walkley, et al., Structural evolution of synthetic alkali-activated CaO-MgO-Na2O-Al2O3-SiO2 materials is influenced by Mg content, Cement and Concrete Research 99 (2017) 155–171.
[73] G.G. Litvan, Variability of the nitrogen surface area of hydrated cement paste, Cement and Concrete Research 6 (1) (1976) 139–143.
[74] S. Walspurger, et al., *High CO2 Storage Capacity in Alkali-Promoted Hydrotalcite-Based Material. In Situ Detection of Reversible Formation of Magnesium Carbonate.* Chemistry–A, European Journal 16 (42) (2010) 12694–12700.
[75] P. Sahoo, et al., Rapid exchange between atmospheric CO2 and carbonate anion intercalated within magnesium rich layered double hydroxide, ACS applied materials interfaces 6 (20) (2014) 18352–18359.
[76] X. Liu, et al., Carbonation behavior of calcium silicate hydrate (CSH): Its potential for CO2 capture, Chemical Engineering Journal 431 (2022), 134243.